

## Development of high intensity focused ultrasound simulator for large-scale computing

Kohei Okita<sup>1,\*</sup>, Kenji Ono<sup>1</sup>, Shu Takagi<sup>2</sup> and Yoichiro Matsumoto<sup>2</sup>

<sup>1</sup>Functionality Simulation and Information Team, VCAD System Research Program, RIKEN,  
2-1 Hirosawa, Wako, Saitama 351-0198, Japan

<sup>2</sup>Department of Mechanical Engineering, The University of Tokyo, 7-3-1 Hongo, Bunkyo, Tokyo 113-8656, Japan

### SUMMARY

High intensity focused ultrasound (HIFU) has been developed as a noninvasive therapeutic option. HIFU simulations are required to support the development of the HIFU device as well as the realization of noninvasive treatments. In this study, an HIFU simulator is developed that uses voxel data constructed from computed tomography scan data on the living human body and signed distance function (SDF) data to represent the object. The HIFU simulator solves the conservation equations of mass and momentum for mixtures with the equation of state for each medium. The numerical method is the finite-difference time-domain method. A high-order finite-difference method based on Lagrange interpolation is implemented to reduce numerical phase error. This approach reproduces wave propagation to an  $n$ th order of accuracy. Representation of the sound source by volume fraction, which is obtained from the SDF using a smoothed Heaviside function, provides around 1.66th order of accuracy in the spherical wave problem. As a realistic application, transcranial HIFU therapy for a brain tumor is modeled, where tissue inhomogeneity causes not only displacement of the focal point but also diffusion of the focused ultrasound. Even in such cases, focus control using phase delays, which are pre-computed based on the time-reversal procedure, enables correct focal point targeting as well as improved ultrasound focusing. Copyright © 2010 John Wiley & Sons, Ltd.

Received 13 July 2010; Revised 23 September 2010; Accepted 24 September 2010

**KEY WORDS:** therapeutic ultrasound; high intensity focused ultrasound (HIFU); numerical simulation; finite-difference time domain (FDTD); signed distance function; parallel computing

### 1. INTRODUCTION

Ultrasound is widely used for diagnostics in therapeutic fields. Ultrasound has been used for cancer treatment, lithotripsy, drug delivery, thrombolysis, and other applications [1]. High intensity focused ultrasound (HIFU) was developed as a noninvasive cancer treatment and may replace surgery in many applications [2]. HIFU is already used in the treatment of prostate cancer and breast cancer, and is a topic of interest in the treatment of deep cancers, such as those of the liver and the brain.

Two major issues concerning application of current HIFU techniques to deep cancers are ultrasound attenuation and focal point displacement. Ultrasound attenuation is problematic because increasing the propagation distance by increasing the ultrasound intensity causes skin burns. Using microbubbles as ultrasonic contrast agents are a solution to this problem; it is well known that the injection of microbubbles enhances tissue heating in HIFU therapy [3], with inertial cavitation playing an important role [4]. Focal point displacement occurs due to the reflection and

\*Correspondence to: Kohei Okita, Functionality Simulation and Information Team, VCAD System Research Program, RIKEN, 2-1 Hirosawa, Wako, Saitama 351-0198, Japan.

†E-mail: okita@riken.jp

refraction of ultrasound at tissue interfaces. Phased array transducers allow for focal point control. The focal point can be assigned to the target by time reversal [5, 6], even if the ultrasound propagates through an inhomogeneous medium, such as the human body. In a basic time-reversal procedure, first ultrasound emitted from a sound source at the target is received by the array transducer. Next, the received signals are reversed and emitted from the array transducer to the target, which focuses the ultrasound on the target correctly. However, in the case of deep cancer, it is difficult to noninvasively put a sound source on the target. A time-reversal process based on prior computed tomography (CT) scans has been proposed as a noninvasive approach [7], where numerical simulations are employed to obtain the signals in the first time-reversal procedure. HIFU simulation can thus predict the location of the focal point of ultrasound propagation through an inhomogeneous medium, supporting accurate control of the array transducer.

Numerical simulations have been applied to many therapeutic ultrasound applications [7–11]. Ultrasound propagation computations most commonly use the finite-difference time domain (FDTD) method [12]. Although the FDTD method allows for conservation of sound energy without numerical dissipation, the numerical phase error increases with increasing propagation distance. In HIFU therapy, the propagation distance is usually around 100 mm from the transducer to the target. For example, when HIFU is applied to a brain tumor, the standing wave of ultrasound in the skull must be taken into account because the standing wave can cause undesirable ablation of normal tissue. To reproduce the standing wave of ultrasound in the skull, the propagation distance becomes 300–600 mm, the distance of 200–300 wavelengths. The wavelength of ultrasound of 1 MHz is around 1.5 mm, given the speed of sound in the human body of around 1500 m/s. In such cases, the phase error is not negligible if second-order differential schemes are applied to empty space. Increasing the number of grid points used to resolve the ultrasound allows for reduction of the phase error, and increasing the number of grid points and the application of higher order differential schemes is required to simulate standing waves in the skull accurately. In practice, however, the required computational resources are not available without access to a supercomputer.

A numerical domain of  $20 \times 20 \times 20$  cm is necessary to include the whole skull. The wavelength of ultrasound of 1 MHz is 1.5 mm, given the speed of sound of around 1500 m/s in soft tissue. When one wavelength is resolved by 15 grid points with grid spacing of 0.1 mm, a cube with 2000 grid points per axis is required to resolve the numerical domain. Such a computation would require around 64 GB of memory (8 bytes times 8 billion grid points) per double precision array variable. If the numerical domain should cover the trunk of the body, far more grid points are needed. HIFU simulation, therefore, requires large-scale computation. The phased array transducer includes many transducer elements distributed in three-dimensional space. The transducer elements should be distinguished from each other to perform focus control using phase delay. To represent many transducer elements in a large-scale computation, a boundary fitted mesh is not suitable because the mesh generation carries a large computational cost and usually requires considerable effort to implement. To avoid such an arduous task, shape representation of objects using the signed distance function (SDF) in a Cartesian mesh is proposed in the present study.

In this article, the basic equations for ultrasound propagation through an inhomogeneous medium are described. We present numerical methods, in particular the shape representation of objects and the implementation of high-order difference schemes. We discuss the results of verification of the numerical methods. Finally, we demonstrate the application of the HIFU simulator, HIFU through a flat plate with an array transducer, and HIFU therapy for brain tumors, including a discussion of focus control in an inhomogeneous medium.

## 2. BASIC EQUATIONS

### 2.1. Ultrasound propagation through an inhomogeneous medium

To represent ultrasound propagation through an inhomogeneous medium, such as the human body, the conservation equations of the mass and momentum for a multicomponent mixture with the equation of state of the medium are described as follows. Because of the small acoustic Mach

number, we can assume adiabatic change of the medium and neglect the advection term during ultrasound propagation. The mass conservation equation for the mixture then becomes

$$\frac{1}{\rho_m c_{sm}^2} \frac{\partial p}{\partial t} + \frac{\partial u_j}{\partial x_j} = 0, \quad (1)$$

where the mixture density,  $\rho_m$ , and the adiabatic speed of sound in mixture,  $c_{sm}$ , are defined in terms of the volume fraction of the medium,  $f_k$ , as  $\rho_m = \sum_k f_k \rho_k$  and  $1/\rho_m c_{sm}^2 = \sum_k f_k / \rho_k c_{sk}^2$  under the assumption of a constant volume fraction. The sound source,  $f_p A \cos(\omega t)$ , is added to the right-hand side of Equation (1) to represent the ultrasound generated by the transducers.

When considering pressure waves with viscous attenuation, the momentum equation is described as

$$\rho_m \frac{\partial u_i}{\partial t} = -\frac{\partial p}{\partial x_i} + \frac{\partial}{\partial x_j} \left\{ \zeta_m e_{kk} \delta_{ij} + 2\mu_m \left( e_{ij} - \frac{1}{3} e_{kk} \delta_{ij} \right) \right\}, \quad (2)$$

where  $e_{ij} = 1/2(\partial u_i / \partial x_j + \partial u_j / \partial x_i)$  is the deformation tensor, and  $\zeta_m$  and  $\mu_m$  are the bulk and shear viscosity, respectively. Here, the constitutive equation for fluid is used, since shear modulus of tissue except for bone is negligibly smaller than bulk modulus. Although bone should be treated as elastic body, bone is modeled as a multicomponent mixture to take into account not shear elasticity but heterogeneities of bones following Aubry *et al.* [7], in fact CT images can give the internal structure of bones. They show that the simulated wave fronts passing through such modeled bones of a skull are very close to the corresponding experimental wave fronts propagation through the skull. The constitutive equation for fluid can be acceptable for discussing the focusing ultrasound through bone. Modeling of bone as anisotropic elastic material will be studied in future to achieve more accurate HIFU simulation.

The nonlinear effect due to material compressibility is higher than that due to the convection terms of continuity and momentum equation depending on the amplitude and nonlinearity coefficient. Tait's equation is employed to take into account the nonlinear effect due to the equation of state of the medium,

$$\rho_k = \rho_{k0} \left( \frac{p + A_{1k}}{p_0 + A_{1k}} \right)^{1/\gamma_k} \quad (3)$$

where  $A_{1k} = \rho_{k0} c_{sk0}^2 / \gamma_k - p_0$  and  $\gamma_k = (B/A)_k + 1$ . Here,  $B/A$  is the nonlinearity coefficient [13, 14]. The density and sonic speed of medium from the Tait's equation are used to obtain the density and sonic speed of mixture.

## 2.2. Perfectly matched layers for nonreflecting boundaries

A perfectly matched layer (PML) [15] is employed to eliminate the reflection of ultrasound at the boundary of a numerical domain. In the region of PML, Equation (1) is split for each component with a damping term by decomposing the pressure as  $p = p_x + p_y + p_z$ :

$$\begin{aligned} \frac{1}{\rho_m c_{sm}^2} \left( \frac{\partial p_x}{\partial t} + \sigma_x p_x \right) + \frac{\partial u}{\partial x} &= 0, \\ \frac{1}{\rho_m c_{sm}^2} \left( \frac{\partial p_y}{\partial t} + \sigma_y p_y \right) + \frac{\partial v}{\partial y} &= 0, \\ \frac{1}{\rho_m c_{sm}^2} \left( \frac{\partial p_z}{\partial t} + \sigma_z p_z \right) + \frac{\partial w}{\partial z} &= 0. \end{aligned} \quad (4)$$

In the same way, the damping term is introduced to the momentum equation without decomposition of the velocity according to PML [15],

$$\rho_m \left( \frac{\partial u_i}{\partial t} + \sigma_i u_i \right) = -\frac{\partial p}{\partial x_i} + \frac{\partial}{\partial x_j} \left\{ \zeta_m e_{kk} \delta_{ij} + 2\mu_m \left( e_{ij} - \frac{1}{3} e_{kk} \delta_{ij} \right) \right\}, \quad (5)$$

where the summation is not taken for  $i$ . The damping coefficient is distributed as a function of the distance  $d_i$  from the boundary of  $x_i = \text{const}$  as follows:

$$\sigma_i(d_i) = \begin{cases} \sigma_{i\max} \left(1 - \frac{d_i}{\delta_{\text{PML}}}\right)^n & \text{for } d_i < \delta_{\text{PML}}, \\ 0 & \text{for } d_i \geq \delta_{\text{PML}}, \end{cases} \quad (6)$$

where  $\sigma_{i\max}$  is the maximum damping coefficient and  $\delta_{\text{PML}}$  is the width of the PML. For  $\sigma_i = 0$ , the sum of components of Equation (4) is equivalent to Equation (1), and also Equation (5) is the same as Equation (2). In fact, instead of Equations (1) and (2), Equations (4) and (5) are solved in the whole numerical domain including the PML by means of Equation (6).

### 3. NUMERICAL METHODS

#### 3.1. Shape representation of objects in Cartesian mesh

Mesh generation of a boundary fitted mesh for a complex shape requires considerable effort to implement. Recently, the immersed boundary method [16] and immersed interface method [17] for Cartesian meshes were developed to simulate flow around an object of a complex shape, represented in the Cartesian mesh as a binary cell, a volume fraction, or a cut cell. In the present study, SDF [18, 19] is employed to represent the object. SDF is used to distinguish between the inside and the outside of the object. The zero isosurface of the SDF represents the surface of the object, and the SDF's gradient at the surface provides the normal vector. The shape representation using SDF is more accurate than that using binary cell or volume fraction. However, when an object designed using computer-aided design (CAD) is introduced to a simulation, generation of SDF of the object in the Cartesian mesh is not a trivial task. RIKEN's VCAD system research program [20], therefore, developed an SDF generation library, V-SDFlib. The V-SDFlib generates the SDF from the surface meshes using the multi-level partition of unity implicits algorithm [21].

As mentioned in Section 2, the volume fraction of an object is employed to evaluate the mixture density and speed of sound. It is difficult to numerically define sharp material interfaces, on Cartesian mesh, with no width or diffusion so that smooth transition or numerical diffusion across the interfaces is initially introduced to treat the interfaces by the governing equations for multicomponent mixture. Thus, the volume fraction is obtained from the SDF through a smoothed Heaviside function [19] as

$$H_\varepsilon(x) = \begin{cases} 0, & x < -\varepsilon, \\ \frac{x + \varepsilon}{2\varepsilon} + \frac{1}{2\pi} \sin\left(\frac{\pi x}{\varepsilon}\right), & |x| < \varepsilon, \\ 1, & \varepsilon < x, \end{cases} \quad (7)$$

where  $\varepsilon$  is a half width of the transient region from 0 to 1. One grid width is chosen as  $\varepsilon$  in this study.

As an example, Figure 1(a) shows the distribution of the SDF of a focusing radiator whose shape is defined using CAD. In Figure 1(b), the distribution of the SDF and the volume fraction of a cross section of the radiator are, respectively, indicated by colored contour lines and grayscale, where the volume fraction changes from one (white) to zero (black) from the inside of the radiator to the outside. In this way, the shape of the radiator can be represented by an SDF in a Cartesian mesh.

#### 3.2. The high order finite-difference method

The FDTD method is employed to compute problems related to wave propagation, such as those for electromagnetic waves, sound waves, and elastic waves, because kinetic energy is numerically conserved during propagation [22]. However, phase error increases with increasing propagation

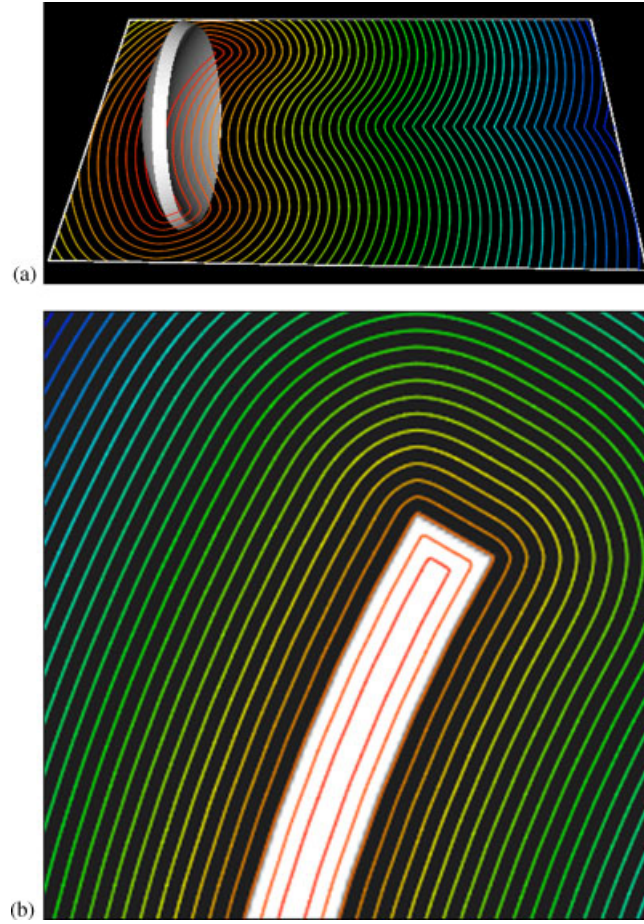


Figure 1. Distribution of the signed distance function (SDF) and volume fraction of a focusing radiator. SDF is generated by V-SDFlib from the shape of the focusing radiator (a) as defined using CAD. The volume fraction of the focusing radiator is obtained from the SDF (b) through the smoothed Heaviside function.

distance. A high order scheme in space is required to reduce the phase error, but the computational cost increases. From the viewpoint of balance between numerical error and computational cost, it is convenient to choose the order of the difference method depending on the problem at hand.

In this study, both difference and interpolation coefficients are defined based on the Lagrange interpolation corresponding to the required accuracy [23] as follows. Scalar variables are the defined cell centers,  $p(x_0 + i\Delta x, y_0 + j\Delta y, z_0 + k\Delta z)$ , and vector components are the defined cell surfaces,  $u(x_0 + \{i + 1/2\}\Delta x, y_0 + j\Delta y, z_0 + k\Delta z)$ , based on the staggered arrangement. Lagrange interpolation from the value at cell center to the value at cell surface is described as

$$\tilde{f}(x_{i+1/2}) = \sum_{k=i-N/2+1}^{i+N/2} \phi_k(x_{i+1/2}) f(x_k), \quad (8)$$

where  $N$  is the number of reference points and  $\phi_k(x)$  is the interpolation coefficient defined by

$$\phi_k(x) = \frac{\pi(x)}{(x - x_k)\pi'(x_k)} \quad (9)$$

with

$$\pi(x) = \prod_{m=1}^N (x - x_m) \quad \text{and} \quad \pi'(x) = \sum_{n=1}^N \prod_{\substack{m=1 \\ m \neq n}}^N (x - x_m). \quad (10)$$

On the other hand, the derivative of Equation (8) can be described as

$$f'(x_{i+1/2}) = \sum_{k=i-N/2+1}^{i+N/2} \phi'_k(x_{i+1/2}) f(x_k). \quad (11)$$

The difference coefficient  $\phi'_k(x)$  then becomes

$$\phi'_k(x) = \frac{(x - x_k)\pi'(x) - \pi(x)}{(x - x_k)^2\pi'(x_k)}. \quad (12)$$

Note that the second derivative is discretized as

$$\begin{aligned} f''(x_m) &= \sum_{i=m-N/2}^{m+N/2+1} \phi'_{i+1/2}(x_m) f'(x_{i+1/2}) \\ &= \sum_{i=m-N/2}^{m+N/2+1} \phi'_{i+1/2}(x_m) \left[ \sum_{k=i-N/2+1}^{i+N/2} \phi'_k(x_{i+1/2}) f(x_k) \right]. \end{aligned} \quad (13)$$

This difference expression of the second derivative is a more accurate approximation than is the derivative of Equation (11).

### 3.3. Time integration

Using the FDTD method, the pressure and velocity are defined at different times as  $p^n = p(t_0 + n\Delta t)$  and  $u_i^{n+1/2} = u_i(t_0 + \{n + 1/2\}\Delta t)$ , respectively. A discretized form of Equation (4) in time is

$$\frac{1}{\rho_m^n c_{sm}^2} \left[ \frac{p_i^{n+1} - p_i^n}{\Delta t} + \frac{\sigma_i}{2} (p_i^{n+1} + p_i^n) \right] + \frac{\partial u_i^{n+1/2}}{\partial x_i} = 0, \quad (14)$$

where the summation is not taken for  $i$ . The momentum equation of Equation (5) is also discretized as

$$\rho_m^n \left[ \frac{u_i^{n+1/2} - u_i^{n-1/2}}{\Delta t} + \frac{\sigma_i}{2} (u_i^{n+1/2} - u_i^{n-1/2}) \right] = -\frac{\partial p^n}{\partial x_i} + \alpha \text{Vis.}^{n+1/2} + (1 - \alpha) \text{Vis.}^{n-1/2}, \quad (15)$$

where the viscous term is

$$\text{Vis.}^{n-1/2} = \frac{\partial}{\partial x_j} \left\{ \zeta_m e_{kk}^{n-1/2} \delta_{ij} + 2\mu_m \left( e_{ij}^{n-1/2} - \frac{1}{3} e_{kk}^{n-1/2} \right) \right\} \quad (16)$$

with  $e_{ij}^{n-1/2} = 1/2(\partial u_i^{n-1/2}/\partial x_j + \partial u_j^{n-1/2}/\partial x_i)$ . The viscosity term is solved either explicitly or implicitly by choosing the coefficient  $\alpha = 0$  or 1. In particular, Equation (15) becomes the Crank–Nicolson second-order scheme for  $\alpha = \frac{1}{2}$ .

### 3.4. Parallel computing

A numerical domain is spatially decomposed to numerical subdomains for parallel computing to balance the load of computation using a Cartesian mesh. Input data is also spatially decomposed into datasets, thus reducing the size of the data corresponding to the number of decompositions. Input data can be prepared independently because of the simple decomposition of the numerical domain as well as the shape representation of SDF in the Cartesian mesh. Therefore, it becomes possible to prepare the input data for large-scale computing even if the size of the input data exceeds the memory capacity of a typical desktop computer.

The decomposed subdomains are allocated to each process, and MPI is employed for data communication between processes running on nodes. Additionally, each process is parallelized by threads using OpenMP. Hybrid MPI/OpenMP is used because Hybrid MPI/OpenMP provides

better scalability than pure MPI, owing to the reduction of extraneous data communications. A super computer, the RIKEN Integrated Cluster of Clusters (RICC), was employed for HIFU simulations. The RICC consists of 1024 nodes with 2 CPUs (4 Cores per CPU) and 12 GB shared memory per node. Hybrid MPI/OpenMP parallel computing is suitable for running code on such computer systems.

#### 4. VERIFICATION OF THE HIFU SIMULATOR

##### 4.1. Periodic wave propagation

Here, we will consider periodic wave propagation to verify implementation of the high-order spatial difference method. The wave equation for the velocity potential  $\phi$  is described as

$$\frac{1}{c_s^2} \frac{\partial^2 \phi}{\partial t^2} - \nabla^2 \phi = 0. \quad (17)$$

The solution of the periodic wave is

$$\phi = \frac{1}{k} (\sin(kx) + \sin(ky) + \sin(kz)) \sin(\omega t), \quad (18)$$

where  $k$  is the wavenumber and  $\omega$  its angular frequency. The pressure and velocity components are obtained from the velocity potential as follows:

$$p = \rho \frac{\partial \phi}{\partial t} = \rho c_s (\sin(kx) + \sin(ky) + \sin(kz)) \cos(\omega t), \quad (19)$$

$$u_i = -\frac{\partial \phi}{\partial x_i} = -\cos(kx_i) \sin(\omega t), \quad (20)$$

where the density  $\rho$  and the speed of sound  $c_s$  are assumed to be constants.

Numerical settings are as follows. The numerical domain is a cube of one wavelength. Periodic boundary conditions are applied to the whole boundary instead of PML. The wave frequency is  $f = 1$  MHz, the density is  $\rho = 1000 \text{ kg/m}^3$ , and the speed of sound is  $c_s = 1500 \text{ m/s}$ . The time increment  $\Delta t$  is chosen to set the CFL number as  $c_s \Delta t / \Delta x = 0.001$ .

After the half-period of the computation, the error of normalized pressure as  $(p_{\text{numerical}} - \tilde{p}_{\text{analysis}}) / \rho c_s$  is examined. The definitions of the  $L_2$  and  $L_{\text{inf}}$  norms are, respectively,

$$L_2 = \sqrt{\frac{\sum_{k=1}^n (p_k - \tilde{p}_k)^2}{n \rho^2 c_s^2}} \quad \text{and} \quad L_{\text{inf}} = \max \left( \left| \frac{p_1 - \tilde{p}_1}{\rho c_s} \right|, \dots, \left| \frac{p_n - \tilde{p}_n}{\rho c_s} \right| \right). \quad (21)$$

The  $L_2$  and  $L_{\text{inf}}$  norms of the error as functions of the normalized grid spacing are shown in Figure 2(a) with comparisons for the various orders of the finite-difference method in space. The  $L_2$  and  $L_{\text{inf}}$  norms of the error as functions of the Courant–Friedrichs–Lewy (CFL) number,  $c_s \Delta t / \Delta x$ , are also shown in Figure 2(b). In the figures, lines are fitted to each result to indicate the power of the normalized grid spacing or CFL number, and the value of the power is shown in the legend. Figure 2(a) clearly shows that the numerical error increases by the order corresponding to the finite-difference method for the second, fourth, and sixth orders in space. On the other hand, the error of the time integration increases by the second power of the CFL number as shown in Figure 2(b). Therefore, it is confirmed that the high order finite-difference method in space is correctly implemented and the time integration method is a second-order scheme in the case of the periodic linear wave propagation without viscous damping.

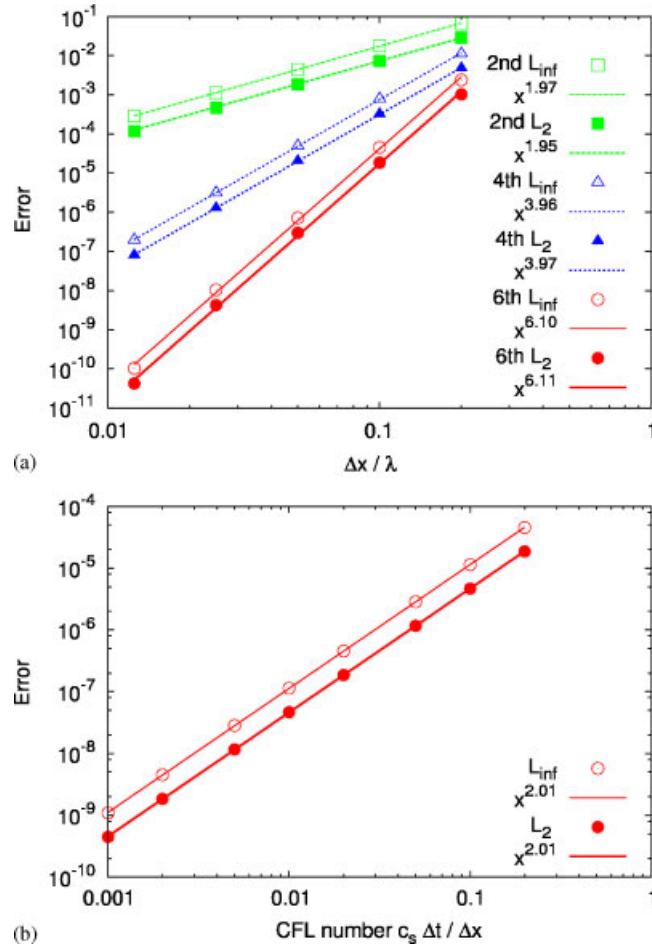


Figure 2.  $L_2$  and  $L_{inf}$  norms of the error of the normalized pressure as a function of (a) the grid spacing (grid dependency) and (b) the CFL number (time dependency). Lines are fitted on each numerical error to indicate the power of functions.

#### 4.2. Spherical wave propagation

Spherical wave propagation is considered as shown in Figure 3. Here, the sound source is not a point but a sphere with finite radius  $R$ . The wave equation for velocity potential is described as

$$\frac{1}{c_s^2} \frac{\partial^2 \phi}{\partial t^2} - \nabla^2 \phi = S(\mathbf{r}) \cos(\omega t), \quad S(\mathbf{r}) = \begin{cases} 1 & \text{for } |\mathbf{r}| \leq R, \\ 0 & \text{for } |\mathbf{r}| > R. \end{cases} \quad (22)$$

Then, the solution of the velocity potential for  $r > R$  is derived [24]

$$\phi(t, r) = \frac{4\pi R^3}{3} \frac{3(\sin(kR) - kR \cos(kR)) \cos(\omega t - kr)}{(kR)^3 4\pi r}. \quad (23)$$

The pressure thus becomes

$$p(t, r) = \rho \frac{\partial \phi}{\partial t} = -\rho c k \frac{4\pi R^3}{3} \frac{3(\sin(kR) - kR \cos(kR)) \sin(\omega t - kr)}{(kR)^3 4\pi r}. \quad (24)$$



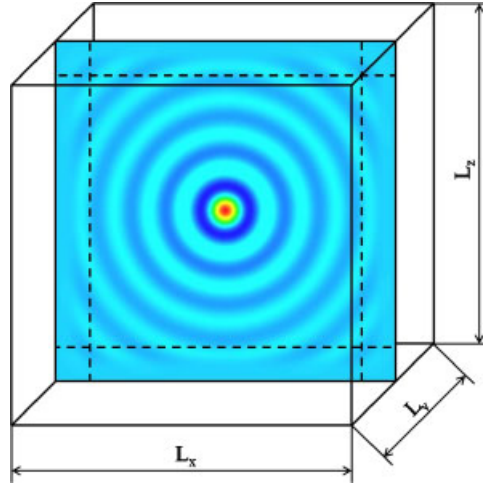


Figure 3. Schematic diagram of the ultrasound propagation from the spherical sound source with finite radius. The numerical domain includes PML inside the whole boundary.

The spherical sound source with finite radius should be added to the right-hand side of Equation (1) for the representation of the problem as

$$\frac{1}{\rho c_s^2} \frac{\partial p}{\partial t} + \nabla \cdot \mathbf{u} = S(\mathbf{r}) \cos(\omega t), \quad S(\mathbf{r}) = \begin{cases} 1 & \text{for } |\mathbf{r}| \leq R, \\ 0 & \text{for } |\mathbf{r}| > R. \end{cases} \quad (25)$$

Since Equation (25) is discretized not in spherical coordinates but in Cartesian coordinates, it is necessary to represent the spherical sound source in a Cartesian mesh. The volume fraction of the spherical sound source can be obtained from the SDF of a sphere of radius  $R$  through a smoothed Heaviside function. Therefore, the accuracy of the shape representation can be examined by solving the problem of spherical wave propagation from a spherical sound source with finite radius.

The numerical settings are as follows. A fourth-order finite-difference scheme is employed in space. The radius of the spherical sound source is  $R = 0.2\lambda$ . The numerical domain is a cube of 10 wavelengths,  $L_x = 10\lambda$ , with a grid resolution of  $\lambda/\Delta x = 10$ . The PML of one wavelength is applied to the whole boundary of the domain. Wave frequency is  $f = 1\text{ MHz}$ , the density is  $\rho = 1000\text{ kg/m}^3$ , and the speed of sound is  $c_s = 1500\text{ m/s}$ . The time increment  $\Delta t$  is chosen to set the CFL number as  $c_s \Delta t / \Delta x = 0.1$ .

The pressure distribution is compared for the small ( $L_x = 10\lambda$ ) and large ( $L_x = 20\lambda$ ) numerical domains as shown in Figure 4(a) to examine the influence of PML, where pressure is normalized by the pressure at radius  $R$ . Both results are in good agreement with the analytical solution indicated by the red line except for both the inside sphere of radius  $R$  and PML from  $r/\lambda = 4$  to 5. Figure 4(b) shows the error of the normalized pressure from  $r/\lambda = 1$  to 4, which is the difference between the results and the analytical solution. The result of the small domain perfectly corresponds with the result of the large domain. Additionally, it is confirmed that PML works well even for diagonal directions. Therefore, the reflection of waves is perfectly eliminated by the PML under the magnitude of the numerical error inside the numerical domain.

We next examine the grid dependency of the solution. Figure 5 shows the  $L_{\text{inf}}$  and  $L_2$  norms of the error of the normalized pressure as functions of the normalized grid spacing by the wavelength, where the epsilon of the width of the smoothed Heaviside function is one grid spacing,  $\varepsilon = \Delta x$ . From the fitted lines,  $L_{\text{inf}}$  increases by the 1.95th power and  $L_2$  by the 1.66th power, even though the finite-difference method is of fourth order.

Figure 6 shows the error of the represented volume of the sphere by the volume fraction as a function of the normalized grid spacing by radius of the sound source. The volume error increases by the 2.01th power of the normalized grid spacing. The volume error is constant if the width of

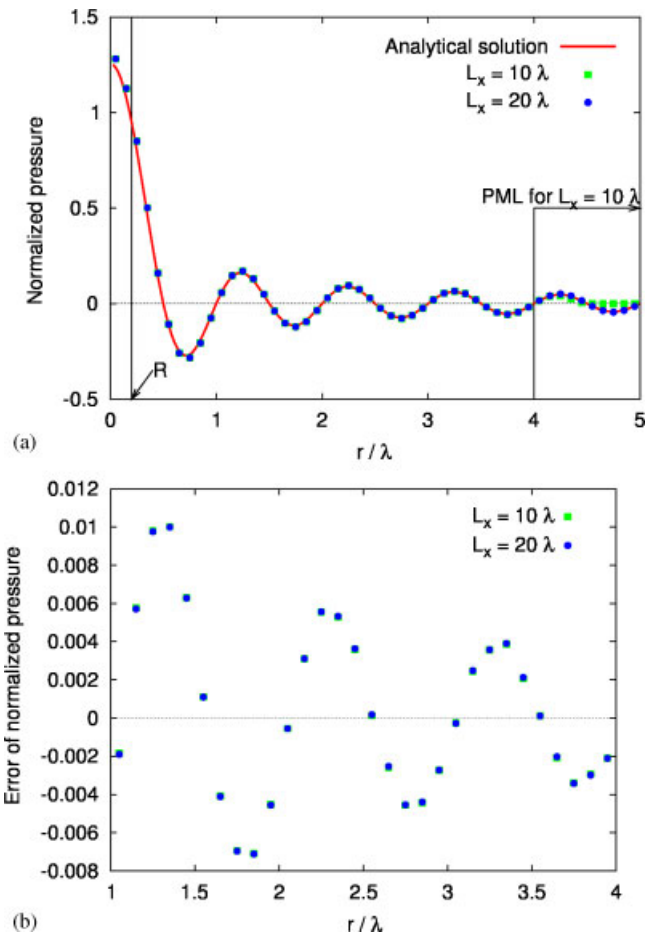


Figure 4. The effect of PML for a nonreflecting boundary. The profiles of normalized (a) pressure and (b) error are compared for two different numerical domain sizes.

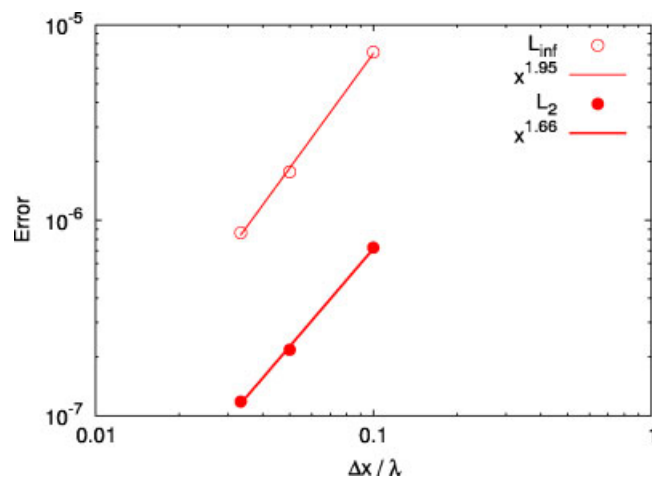


Figure 5.  $L_{\infty}$  and  $L_2$  norms of the error of normalized pressure as a function of the normalized grid spacing for  $\varepsilon = \Delta x$ .

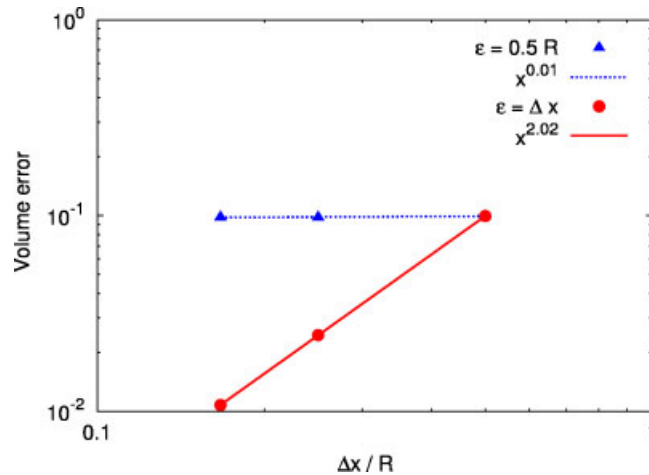


Figure 6. Error of the volume of the sphere source as a function of the normalized grid spacing by radius.

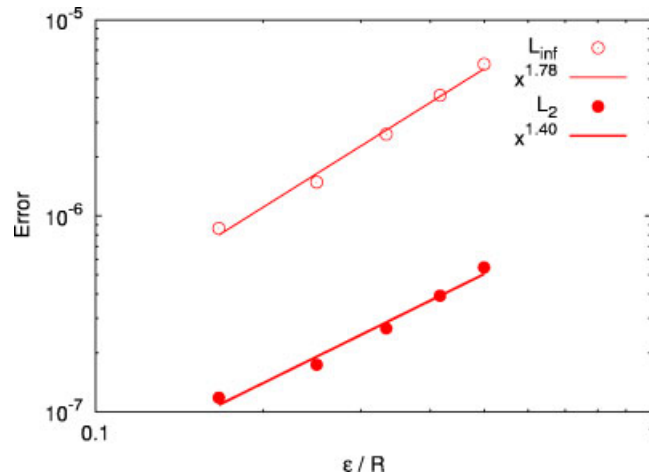


Figure 7. Influence of the width of the smoothed Heaviside function on the numerical error.  $L_{\text{inf}}$  and  $L_2$  are norms of the error of normalized pressure as a function of the normalized width of the smoothed Heaviside function in the case of a constant grid resolution of  $\lambda/\Delta x = 30$ .

the smoothed Heaviside function is fixed as  $\varepsilon/R = 0.5$ . Therefore, the volume error mainly depends on the width of the smoothed Heaviside function.

We next examine the influence of the width of the smoothed Heaviside function, that is, the distribution of the sound source, on the numerical error. Figure 7 shows the  $L_2$  and  $L_{\text{inf}}$  norms of the errors of the normalized pressure as function of the normalized width of the smoothed Heaviside function by radius of the spherical sound source, where the grid resolution of the wave is a constant,  $\lambda/\Delta x = 30$ . Numerical errors  $L_{\text{inf}}$  and  $L_2$ , respectively, increase by the 1.78th and 1.40th power of the normalized width. As shown in Figure 6, the volume error increases by the 2.01th power of the normalized grid spacing. Since the numerical errors respectively increase by the 1.95th and 1.66th power of the normalized grid spacing, as shown in Figure 5, the grid dependency of the numerical errors for  $\varepsilon = \Delta x$  is due not only to the volume error but also to the distribution error of the volume fraction. Therefore, the high grid resolution of the sphere sound source is required to reduce the numerical error, because the width of the smoothed Heaviside function is dependant on the grid spacing.

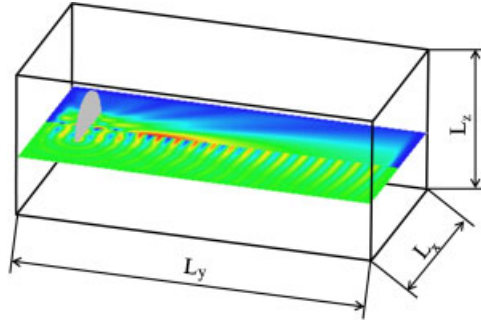


Figure 8. Schematic diagram of the simulation ultrasound radiation from a circular piston with radius  $\alpha = 2\lambda$ . The size of the numerical domain is  $10\lambda \times 20\lambda \times 10\lambda$ . Instantaneous pressure and pressure amplitude on a cross section are shown.

#### 4.3. Circular piston

As mentioned in the above two sections, the propagation of linear waves can be solved by the order of accuracy corresponding to the finite-difference schemes of the second, fourth, and sixth orders, and the accuracy due to the shape representation is an order of around 1.66. Here, the ultrasound field radiated by a circular piston as shown in Figure 8 is considered as a more realistic problem to verify the numerical method of this study. The solution of the ultrasound field radiated by a circular piston [25] is

$$p(r, z) = -j\omega\rho v e^{j\omega t} \frac{a}{jk\pi} \int_0^\pi \frac{r \cos\psi - a}{r^2 + a^2 - 2ar \cos\psi} \times (e^{-jk\sqrt{r^2 + a^2 - 2ar \cos\psi + z^2}} - e^{-jkz}) d\psi. \quad (26)$$

The circular piston is represented by a sound source of finite width. The velocity amplitude of the circular piston  $v$  is related to the source amplitude  $Q_s$  and the thickness of the plate  $t_s$  as

$$v = Q_s t_s \frac{\sin(kt_s)}{kt_s}. \quad (27)$$

Numerical settings are as follows. The radius of the circular piston is  $\alpha = 2\lambda$ . The size of the numerical domain is  $10\lambda \times 20\lambda \times 10\lambda$  and is resolved by  $100 \times 200 \times 100$  grid points with a grid resolution of  $\lambda/\Delta x = 20$ . The PML of one wavelength is applied to the whole boundary of the domain. The wave frequency is  $f = 1$  MHz. The density and speed of sound are, respectively, constants of  $\rho = 1000 \text{ kg/m}^3$  and  $c_s = 1500 \text{ m/s}$ . The time increment  $\Delta t$  is chosen to set the CFL number as  $c_s \Delta t / \Delta x = 0.1$ .

Figure 9 shows the instantaneous pressure and maximum pressure distributions of the numerical results, compared with the analytical solution of Equation (26), where contour lines of the analytical solution and the numerical result are shown in left and right of each figure. Both distributions of the numerical results qualitatively agree with the analytical solutions.

To compare the result with the analytical solution quantitatively, the instantaneous pressure and maximum pressure profiles on the axis are, respectively, indicated in Figure 10. In these figures, the results of a coarse grid resolution,  $\lambda/\Delta x = 10$ , are also plotted to show the grid dependency. The numerical results are in good agreement with the analytical solution. The pressure amplitude of the first peak around  $z/\lambda = 0.5$  in the numerical result is slightly higher than that in the analytical solution. The peak amplitude increases with decreased grid spacing. The result of a thinner plate provides better agreement with the analytical solution than the result of the thicker plate (data not shown). Therefore, since the analytical solution assumes a zero thickness circular plate, the difference of the pressure amplitude of the first peak between the numerical result and the analytical solution is not due to the grid resolution but due to the thickness of the circular piston. That is, the radiation from the end face of circular plate affects the pressure distribution. Although the numerical result can approach the analytical solution by decreasing the thickness corresponding to the grid resolution, the results with finite thickness are accurate enough to discuss the ultrasound

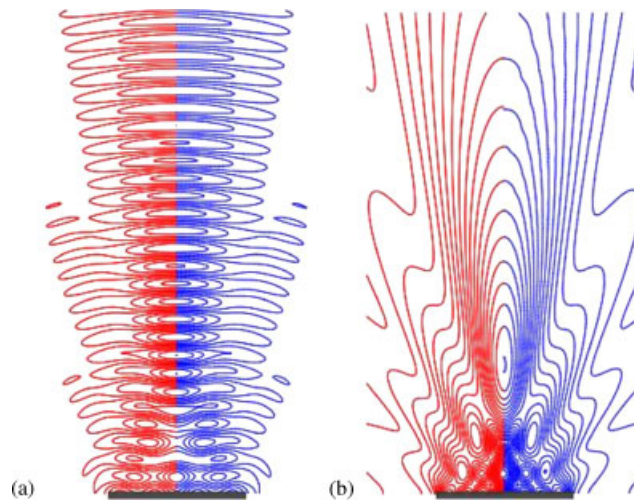


Figure 9. Distribution of (a) instantaneous pressure and (b) maximum pressure. Contour lines of the analytical solution (red) and the numerical result (blue) are compared in left and right of each figure.

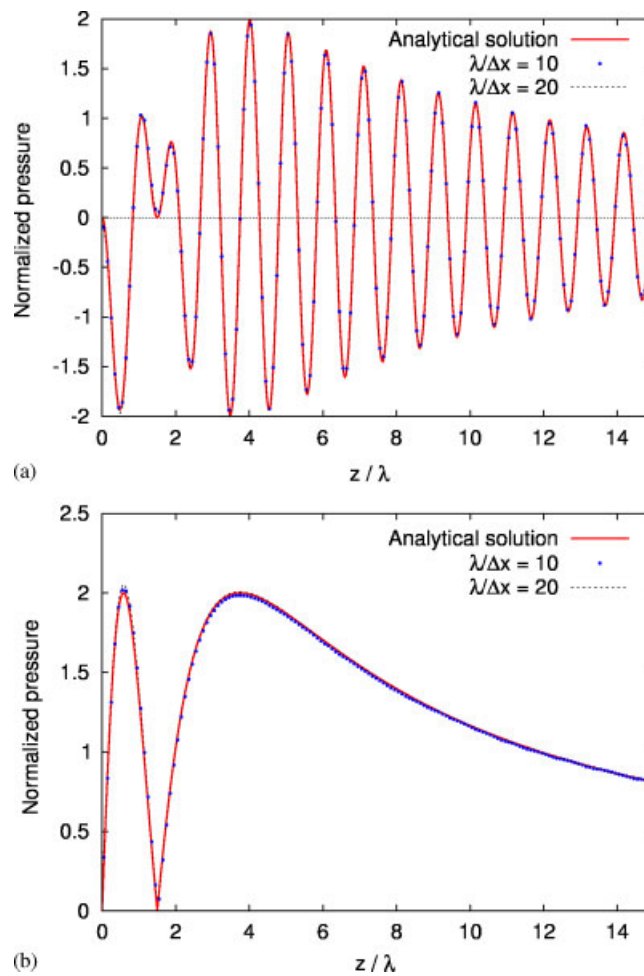


Figure 10. Influence of grid resolution on the profile of (a) instantaneous pressure and (b) maximum pressure on the axis.

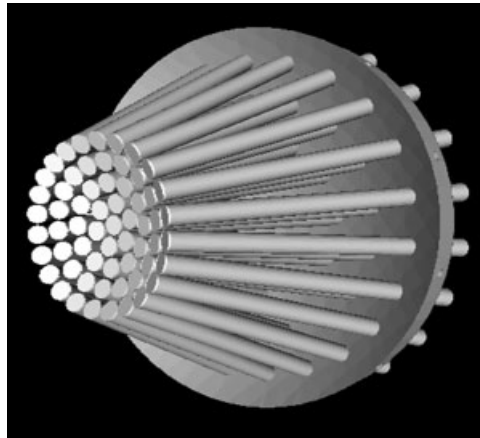


Figure 11. An array transducer consists of 61 pen type transducers with diameter of 10 mm. Geometrical focal distance of the array transducer is 85 mm.

field radiated by the circular piston. In addition, we compared the ultrasound field of a focusing radiator [26] to verify the numerical simulation, and obtained similar results [27].

## 5. FOCUS CONTROL BY AN ARRAY TRANSDUCER

### 5.1. Numerical setup

We employed an array transducer as shown in Figure 11 for the following computation. The array transducer includes 61 pen type transducer elements with diameter of 10 mm. The focal distance of the array transducer is 85 mm. Figure 12(a) shows a simplified model of the array transducer and the numerical domain. The numerical domain is decomposed into 32 ( $2 \times 4 \times 4$ ) numerical subdomains for parallel computing. Numerical subdomains include the transducer elements of the array transducer. Because it is necessary to distinguish between the transducer elements to realize phase control, each transducer element is represented by the local volume data of each SDF as shown in Figure 12(b). The size of the numerical domain is  $120 \times 160 \times 120$  mm, which is divided into  $600 \times 800 \times 600 = 288\,000\,000$  grid points. The grid spacing is 0.2 mm, which resolves the wavelength of ultrasound of 1 MHz in water in around 7.5 grid points. The time increment  $\Delta t$  is configured to set the CFL number of  $c_s \Delta t / \Delta x = 0.1$ . Computation of 10 000 time steps takes around 2 h using 32 CPUs (128 cores) on the RICC, when the fourth-order finite-difference scheme in space and explicit integration ( $\alpha = 0$ ) of the viscous terms are chosen.

### 5.2. Ultrasound radiated by the array transducer

Propagation of ultrasound radiated by the array transducer in water is simulated by the HIFU simulator. The instantaneous pressure distribution is visualized by the volume rendering method to show high and low pressure regions as shown in Figure 13(a). The probe in the figure indicates the location where the ultrasound is focused at the geometric focus of the array transducer. The volume rendering method also provides a visualization of the maximum pressure distribution, as shown in Figure 13(b). The high pressure amplitude region corresponding to the focal point is shown as a grain shape. The focal point is located at the geometric focus because the ultrasound propagates through a homogeneous medium of water. Figure 13(c) shows the maximum and instantaneous pressure profile on the axis. The peak pressure at the focal point reaches 7.0 MPa. The absolute value of the maximum pressure at the focal point is greater than that of the minimum pressure at the focal point because the equation of state becomes nonlinear with increasing pressure amplitude.

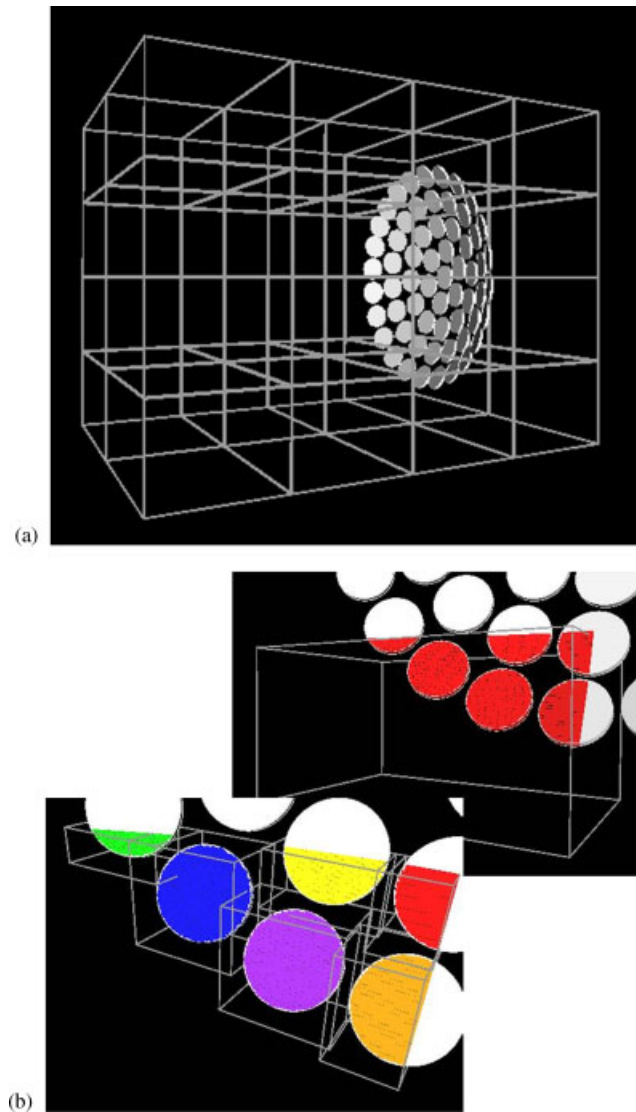


Figure 12. A simplified model of the array transducer with a numerical domain (a) which is decomposed into subdomains for parallel computing. A numerical subdomain (b) includes transducer elements (upper) that are represented by the local volume data to distinguish each transducer (lower).

### 5.3. Focusing ultrasound through a plate

Here, to examine the focus control in an inhomogeneous medium, we consider the ultrasound propagation through a plate in water, as shown in Figure 14. The plate is placed 20 mm away from the transducer. The plate's thickness is 5 mm, its density is  $1380 \text{ kg/m}^3$ , and its acoustic impedance of 3.75 MRayl, each value corresponding to the physical properties of bone [14].

Figure 15 shows the distribution of instantaneous pressure and maximum pressure, as well as an axial profile of ultrasound propagation through the plate in water. The ultrasound focuses away from the target toward the transducer because the speed of sound in the plate is faster than the speed of sound in water. Additionally, the secondary peak pressure inside the plate at  $y=60\text{--}65 \text{ mm}$  and the standing waves between the plate and the transducer at  $y=65\text{--}85 \text{ mm}$  are observed. The peak pressure at the focal point is 4.7 MPa, which is 33% less than the peak pressure of 7 MPa in the case without the plate. The position of the peak pressure moves approximately 7 mm away from the target.



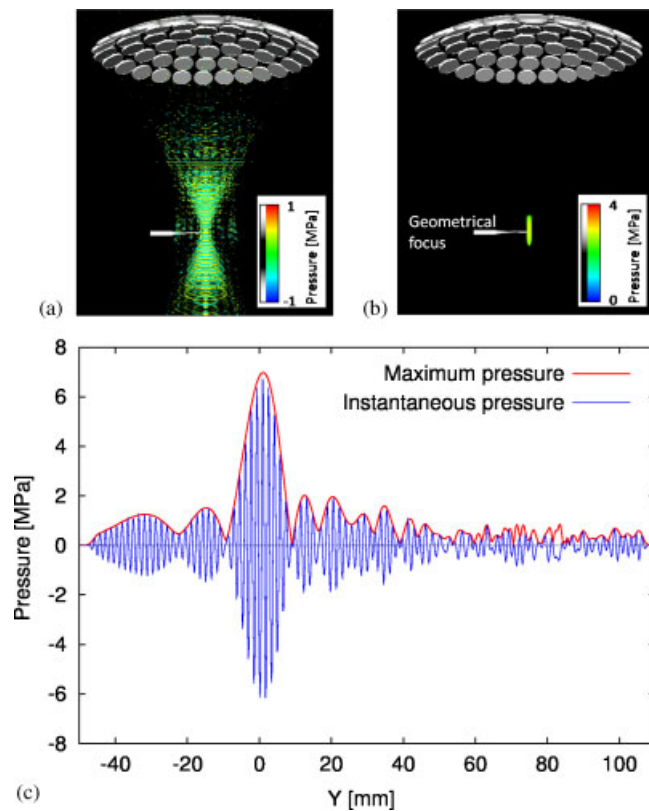


Figure 13. Ultrasound field generated by the array transducer in water: (a) Instantaneous pressure; (b) maximum pressure; and (c) pressure profile on axis.

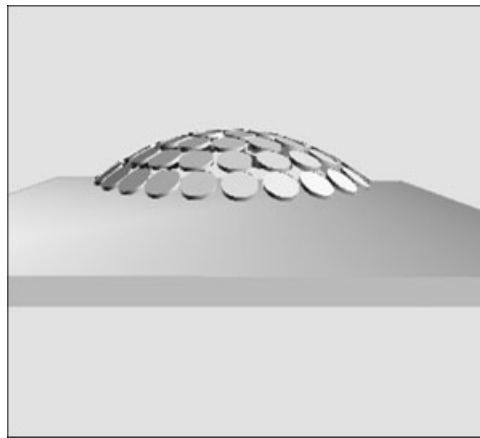


Figure 14. Schematic diagram of the ultrasound propagation through a plate in water. The 5-mm-thick plate is placed 20 mm away from the array transducer.

When the ultrasound propagates through a homogeneous medium of water, the focal point can be assigned to the target by controlling the phase delay of the array transducer, which is easily obtained through a simple calculation by dividing the distance between a target and transducer elements at the constant speed of sound in water. In the simple case of focusing ultrasound through the plate, it is sufficient to assign the focal point to the target by mechanical movement of the array transducer or the phase delay, relocating the focal point beyond the geometrical focus. When



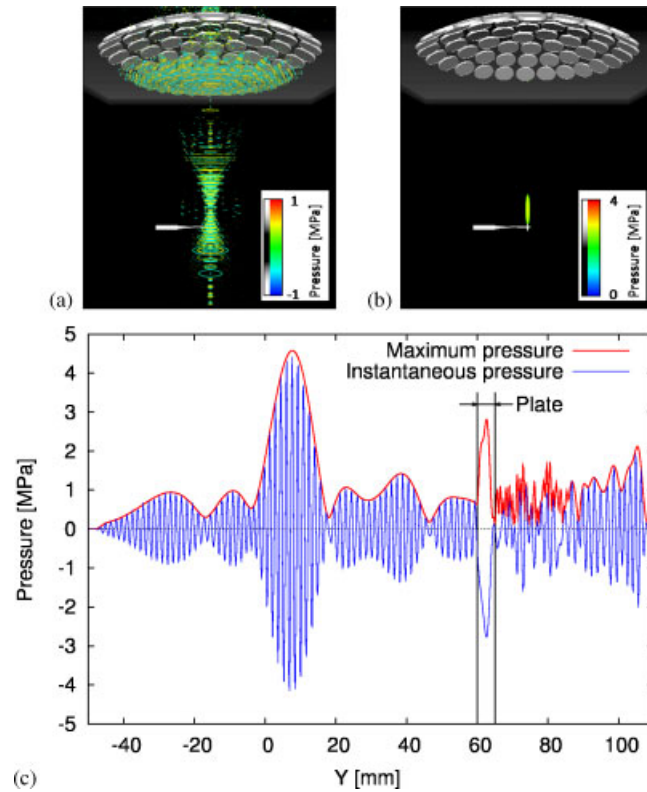


Figure 15. Ultrasound propagation through the plate in water without focus control: (a) Instantaneous pressure; (b) maximum pressure; and (c) pressure profile on axis.

ultrasound propagates through an inhomogeneous medium, such as a human body, however, it is difficult to obtain an appropriate phase delay that will assign the focal point to the target. Time reversal [6] is a solution to this problem and enables one to assign the focal point to the target correctly, even if the ultrasound propagates through an inhomogeneous medium such as the human body. The basic time reversal procedure is as follows. First, the emitted ultrasound from a sound source at the target is received by the array transducer. Next, the received signal is reversed and emitted from the array transducer. Then, the ultrasound is focused on the target correctly.

Based on the basic time reversal procedure, an estimation method of the phase delay using pre-computation is as follows. First, ultrasound is emitted from a sound source at the geometrical focal point as a target point, and is received by the array transducer as shown in Figure 16(a). Figure 16(b) shows the profiles of received signals at the center transducer element and one of the outer transducer elements, in which both the phase and the amplitude of pressure do not correspond, owing to the propagation through the inhomogeneous medium. Next, the following equation is used to create cross-correlations of pressure profiles of every transducer element with that of the center transducer element, which is used as a reference transducer element:

$$p_{\text{center}} \cdot p_n(\tau) = \int p_{\text{center}}(t) p_n(t + \tau) dt. \quad (28)$$

The phase delay  $\tau$  is chosen as the cross-correlation maximum, as shown in Figure 16(c). Then, a map of the phase delay for each element is obtained as shown in Figure 16(d), where the identified number of the transducer element is numbered clockwise from the center to the outer elements. The phase delays are classified into five groups corresponding to their distance from the center. Although the phase delays in each group should be equivalent, the phase delays include

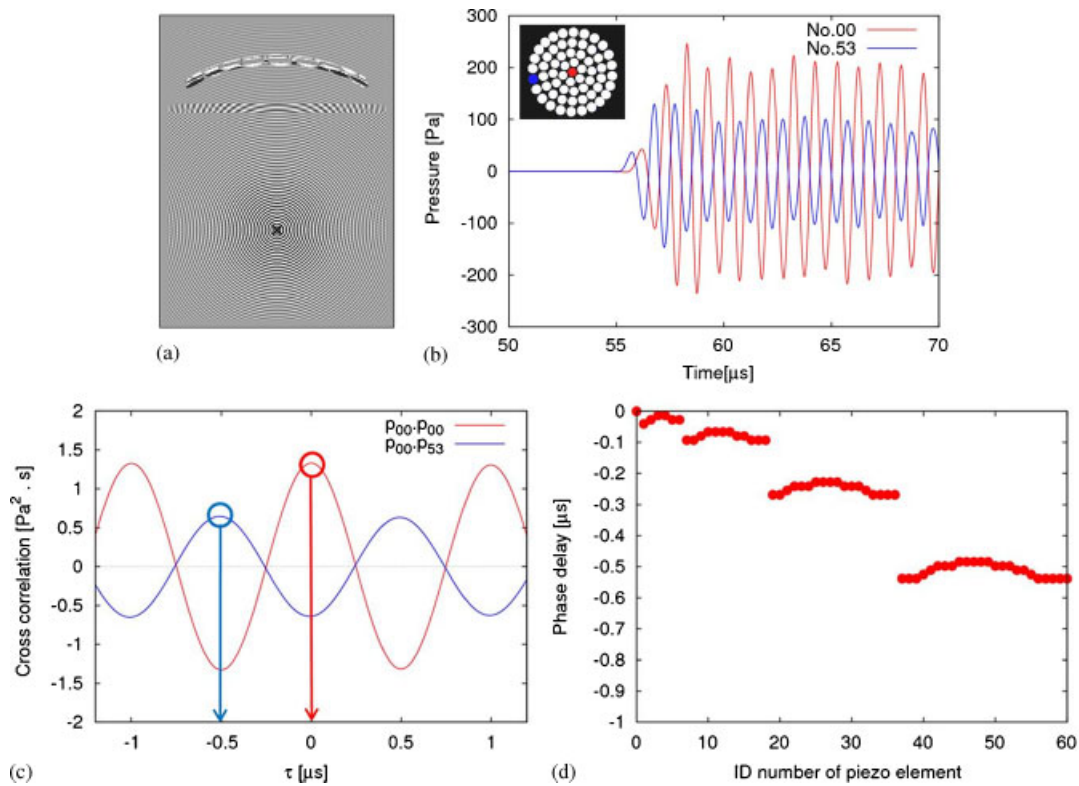


Figure 16. Estimation of phase delays by pre-computation based on the time reversal: (a) Emitted ultrasound from the target is received by the array transducer; (b) Received pressure profiles at the center and outer elements; (c) Cross correlation of pressure profiles; and (d) Phase delay map.

disturbances due to numerical error. In view of the fact that one wave is resolved in 7.5 grid points, however, the simulation is reasonable because the disturbance in the phase delays is less than the time of one period divided by 7.5.

The result of focus control by means of the phase delay map is shown in Figure 17. The ultrasound is focused on the target through the plate, and the focal point is assigned to the target correctly. Figure 18 compares the pressure profiles with and without focus control by phase delay. The peak pressure with focus control is 4.2 MPa, which is 11% less than the peak pressure of 4.7 MPa without the focus control. Focus control moves the position of the focal point 7 mm toward the target. Thus, the phase delay map estimated by time reversal pre-computation enables correct assignment of the focal point to the target.

## 6. HIFU THERAPY FOR BRAIN CANCER WITH AN ARRAY TRANSDUCER

### 6.1. Modeling the human body

The voxel model of the human body was constructed as part of the RIKEN Computational Biomechanics Project by stacking CT images as shown in Figure 19. The voxel model includes the CT number (the Hounsfield unit), and is not directly used for numerical simulations. Some conversion from the Hounsfield unit is required. In this study, the volume fraction of bone is estimated from the Hounsfield unit as follows. The Hounsfield unit is defined as

$$H = 1000 \frac{\mu_x - \mu_{\text{water}}}{\mu_{\text{bone}} - \mu_{\text{water}}}, \quad (29)$$

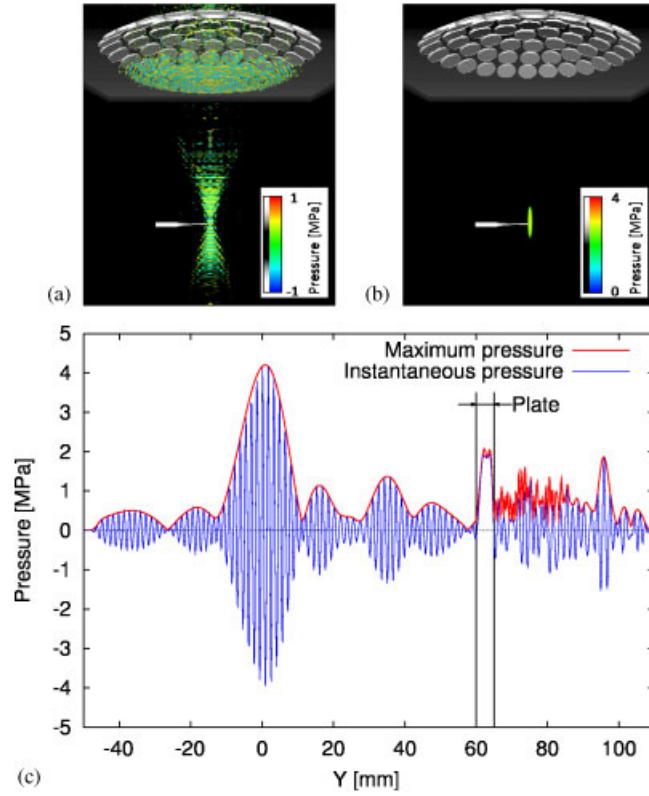


Figure 17. Ultrasound propagation through the plate in water with focus control: (a) Instantaneous pressure; (b) maximum pressure; and (c) pressure profiles on axis.

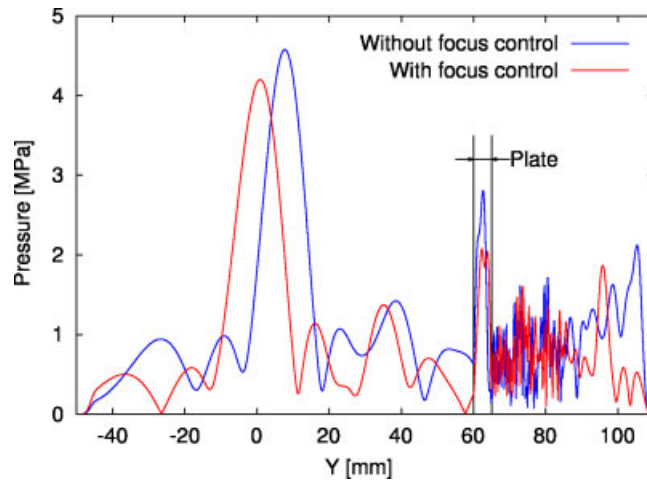


Figure 18. Comparison of the pressure profiles on the axis with and without focus control by the phase delay.

where  $\mu$  is the photoelectric linear attenuation coefficient. We assume that the local photoelectric linear attenuation coefficient is represented as a function of the volume fraction of bone [7],  $\mu_x = \mu_{\text{bone}} f_B + \mu_{\text{water}}(1 - f_B)$ . Substituting  $\mu_x$  in Equation (29) gives the relationship between volume fraction of bone and the Hounsfield unit as

$$f_B = \frac{\mu_x - \mu_{\text{water}}}{\mu_{\text{bone}} - \mu_{\text{water}}} = \frac{H}{1000}. \quad (30)$$

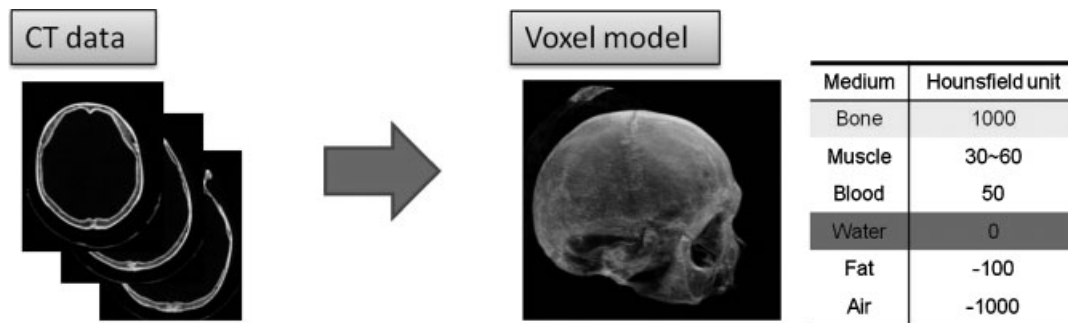


Figure 19. Construction of the three-dimensional computational model of the human body from CT images.

A three-dimensional computational model of human body is then constructed by stacking CT images of a living human body with the conversion from Hounsfield units to volume fraction of bone.

### 6.2. Numerical settings

Figure 20 shows a voxel model of a part of a human skull, visualized using the volume rendering method of V-Isio [20]. The array transducer is arranged relative to the skull as shown in Figure 20. The array transducer is surrounded by a numerical domain of size  $120 \times 160 \times 120$  mm, and is resolved by  $600 \times 800 \times 600$  meshes with grid spacing of 0.2 mm. One wavelength of 1.5 mm for ultrasound of 1 MHz in water is resolved with 7.5 grid points. The voxel model of the skull is divided into cubes of 1 mm. The volume fraction of the bone at a grid point of the numerical domain is interpolated from the voxel model of the skull by trilinear interpolation. The distribution of the volume fraction of bone at a cross section in the numerical domain is also shown in Figure 20. The density of the brain is  $1040 \text{ kg/m}^3$ , and the speed of sound in brain tissue is 1560 m/s. The viscosity of the brain is assumed to be  $0.274 \text{ Pa}\cdot\text{s}$  from the viscosity of water, based on the ratio of the attenuation coefficient between brain tissue and water. On the other hand, bone has a density of  $1920 \text{ kg/m}^3$ , and the speed of sound therein is 3635 m/s. Bone is assumed to have zero viscosity. The distributions of the mixture density and speed of sound are related to the volume fraction of bone as mentioned in Section 2.

### 6.3. Focusing ultrasound through the skull

Figure 21 shows ultrasound propagation through the skull without focus control. As shown in Figure 21(a), ultrasound propagates through the skull and focuses away from the target. The inhomogeneity of the skull causes a complex ultrasound field. High pressure fluctuations occur in the skull, which causes unexpected heating of the bone. The skull transmits ultrasound well in a particular direction. As shown in Figure 21(b), the focal point is diffused and not on target. The peak pressure at the focal point is 2.50 MPa, 64% less than the peak pressure of 7.0 MPa in water. The attenuation of the ultrasound is due to the reflection and refraction of ultrasound in the skull and viscous damping in the brain, the viscosity of which is much higher than that of water.

Both position control of the focal point and the improved focusing are required in this case. Mechanical movement of the focal point does not improve the diffusion. Only phase control can achieve improved focusing when ultrasound propagates through an inhomogeneous medium. Pre-computed focus control as described in Section 5 is, therefore, applied to focusing ultrasound through the skull. The instantaneous pressure and maximum pressure distributions are shown in Figure 22. Ultrasound propagates through the skull and is focused on the target. As shown in Figure 22(b), the focal point is concentrated and assigned to the target correctly. The peak pressure of the focal point reaches 3.10 MPa, which is 24% higher than that without focus control. Because the heating effect is related to the square of the pressure amplitude, the heating effect is improved

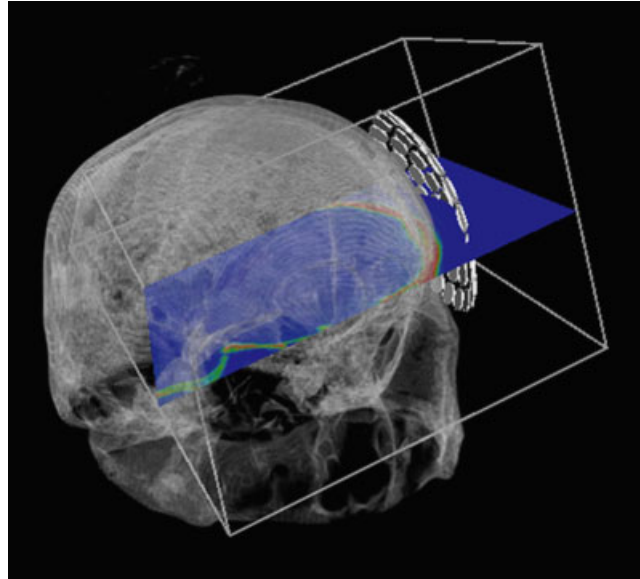


Figure 20. Voxel model of human skull and the array transducer bounded by the numerical domain. The colored contour of the cross section represents the distribution of the volume fraction of bone. The numerical domain is  $120 \times 160 \times 120$  mm and is resolved by  $600 \times 800 \times 600$  grid points with grid spacing of 0.2 mm.

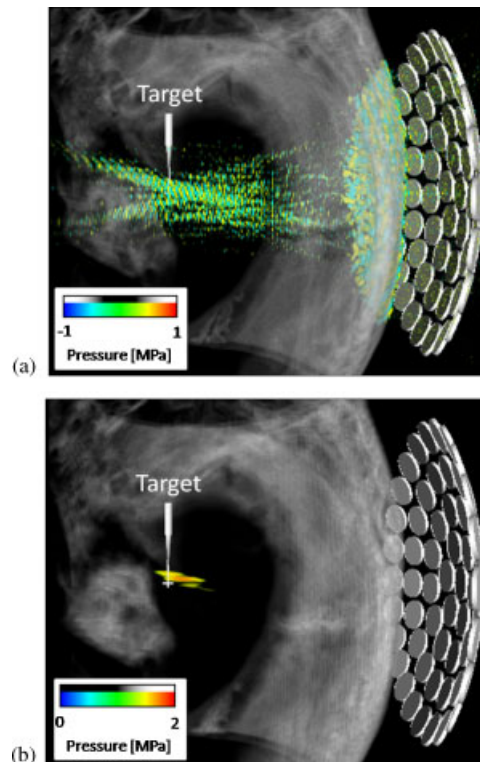


Figure 21. Focusing ultrasound propagation through the human skull using an array transducer without focus control. Distribution of the instantaneous pressure and maximum pressure is visualized with the skull bone: (a) Instantaneous pressure; and (b) Maximum pressure ( $p_{\max} = 2.50$  MPa).

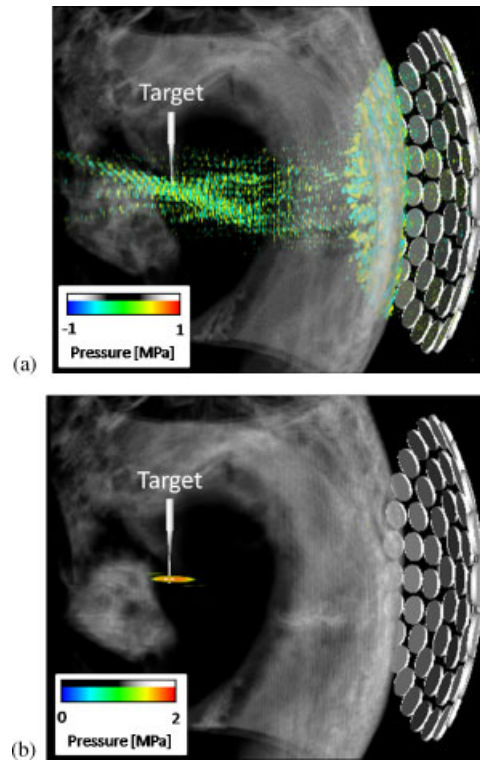


Figure 22. Focusing ultrasound propagation through the human skull using an array transducer with focus control. Distribution of the instantaneous pressure and maximum pressure is visualized with the skull bone: (a) Instantaneous pressure and (b) Maximum pressure ( $p_{\max} = 3.10 \text{ MPa}$ ).

by 54%. Thus, the focus control places the focal point at the target, and furthermore provides efficient heating due to the improved focusing.

## 7. CONCLUSION

The HIFU simulator, which is based on both CT images of the living human body and objects defined by CAD, was developed as shown in Figure 23. In particular, the SDF is used for shape representation of objects in a Cartesian mesh rather than a boundary fitted mesh, thus enabling the preparation of input data for large-scale parallel computing, both because mesh generation is not required and because the domain decomposition of Cartesian meshes is simple. In addition, the high order finite-difference method using Lagrange interpolation was implemented to reduce numerical phase error caused by the long propagation distance and low grid resolution.

The HIFU simulator was verified for problems, such as the periodic wave, the spherical wave from a finite sphere, and ultrasound radiation from a circular piston. The numerical accuracy of the wave propagation corresponds to the second, fourth, and sixth order of the finite-difference method. Using a PML as a nonreflecting boundary condition works well to remove reflection waves lower than the magnitude of the numerical error inside the numerical domain. The representation of the sound source by volume fraction, which is obtained from an SDF through a smoothed Heaviside function, provided a 1.66th order of accuracy in the spherical wave problem. The ultrasound field radiated from the circular piston was in close agreement with the analytical solution. Thus, the HIFU simulator provides sufficient numerical accuracy to describe the ultrasound field.

HIFU through a plate with the array transducer was reproduced numerically. The focus control by phase delay, which was estimated from time reversal-based pre-computation, enabled accurate



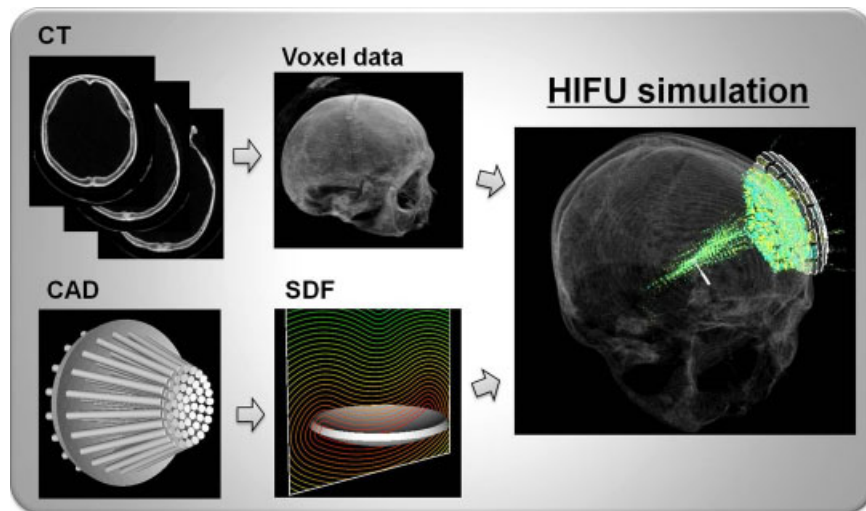


Figure 23. Schematic diagram of the data flows to the HIFU simulator: volume data constructed from CT data of a living human body and the volume data of the signed distance function (SDF) representing an object defined by CAD are employed for an HIFU simulation.

focal point placement at the target even when the ultrasound propagated through an inhomogeneous medium.

As a realistic application, transcranial HIFU therapy for a brain tumor was modeled well by the HIFU simulator, where inhomogeneity caused not only displacement of the focal point but also diffusion of the focusing ultrasound. Even in such cases, phase control based on pre-computation was highly effective for solving both problems.

#### ACKNOWLEDGEMENTS

Part of this study was supported by the 'Research and Development of the Next-Generation Integrated Living Matter Simulation' project of the Ministry of Education, Culture, Sports, Science and Technology. The calculations were performed using the RIKEN Integrated Cluster of Clusters (RICC).

#### REFERENCES

1. Duck FA, Baker AC, Starritt HC. *Ultrasound in Medicine*. Medical Science Series. Institute of Physics Publishing: Bristol and Philadelphia, 1998.
2. Kennedy JE, ter Haar GR, Cranston D. High intensity focused ultrasound: surgery of the future? *The British Journal of Radiology* 2003; **76**:590–599.
3. Umemura S, Kawabata K, Sasaki K. In vivo acceleration of ultrasonic tissue heating by microbubble agent. *IEEE Transactions on Ultrasonics, Ferroelectrics, and Frequency Control* 2005; **52**:1690–1698.
4. Coussios CC, Roy RA. Applications of acoustic and cavitation to noninvasive therapy and drug delivery. *Annual Review of Fluid Mechanics* 2008; **40**:395–420.
5. Fink M. Time reversal of ultrasonic fields. Part I: Basic principles. *IEEE Transactions on Ultrasonics, Ferroelectrics, and Frequency Control* 1992; **39**(5):555–566.
6. Fink M, Montaldo G, Tanter M. Time-reversal acoustics in biomedical engineering. *Annual Review of Biomedical Engineering* 2003; **5**:456–497.
7. Aubry J-F, Tanter M, Pernot M, Tomas J-L, Fink M. Experimental demonstration of noninvasive transskull adaptive focusing based on prior computed tomography scans. *Journal of the Acoustical Society of America* 1993; **113**(1):84–93.
8. Sun J, Hynynen K. Focusing of therapeutic ultrasound through a human skull: a numerical study. *Journal of the Acoustical Society of America* 1998; **104**(3):1705–1715.
9. Curra FP, Mourad PD, Khokhlova VA, Cleveland RO, Crum LA. Numerical simulations of heating patterns and tissue temperature response due to high-intensity focused ultrasound. *IEEE Transactions on Ultrasonics, Ferroelectrics, and Frequency Control* 2000; **47**(4):1077–1089.
10. Hariharan P, Myers MR, Banerjee RK. HIFU procedures at moderate intensities-effect of large blood vessels. *Physics in Medicine and Biology* 2007; **52**:3493–3513.

11. Baron C, Aubry J-F, Tanter M, Meairs S, Fink M. Simulation of intracranial acoustic fields in clinical trials of sonothrombolysis. *Ultrasound in Medicine and Biology* 2009; **35**(7):1148–1158.
12. Yee KS. Numerical solution of initial boundary value problems involving Maxwell's equations in isotropic media. *IEEE Transactions on Antennas and Propagation* 1966; **14**(8):302–307.
13. Naugolnykh K, Ostrovsky L. *Nonlinear Wave Processes in Acoustics*. Cambridge University Press: Cambridge, 1998; 1–36.
14. International Commission on Radiation Units and Measurements. *Tissue Substitutes, Phantoms and Computational Modelling in Medical Ultrasound*. ICRU Report 61, 1998; 43–51.
15. Berenger JP. A perfectly matched layer for the absorption of electromagnetic waves. *Journal of Computational Physics* 1994; **114**:185–200.
16. Mittal R, Iaccarino G. Immersed boundary methods. *Annual Review of Fluid Mechanics* 2005; **37**:239–261.
17. Li Z, Ito K. *The Immersed Interface Method*. SIAM: Philadelphia, PA, 2006.
18. Sethian JA. *Level Set Methods and Fast Marching Methods*. Cambridge University Press: Cambridge, 1999.
19. Osher S, Fedkiw R. *Level Set Methods and Dynamic Implicit Surfaces*. Springer: New York, 2003.
20. VCAD System Research Program. Available from: <http://www.vcad-hpsv.riken.jp>.
21. Ohtake Y, Belyaev A, Alexa M, Turk G, Seidel H-P. Multi-level partition of unity implicit surfaces. *ACM Transactions on Graphics* 2003; **22**(3):463–470.
22. Hairer E, Lubich C, Wanner G. *Geometric Numerical Integration*. Springer: Berlin, Heidelberg, 2002.
23. Kajishima T. *Numerical Simulation of Turbulent Flows*. YOKENDO: Tokyo, 1999 (in Japanese).
24. Sugiyama K. Private communication.
25. McGough RJ, Samulski TV, Kelly JF. An efficient grid sectoring method for calculations of the near-field pressure generation by a circular piston. *Journal of the Acoustical Society of America* 2004; **115**:1942–1954.
26. O'Neil HT. Theory of focusing radiators. *Journal of the Acoustical Society of America* 1949; **21**:516–526.
27. Leduc N. Focus control of high intensity focused ultrasound for medical applications. Master Thesis, The University of Tokyo, 2010.